Holographic surface-acoustic-wave tweezers for functional manipulation of solid or liquid objects

Peng-Qi Li,[1] Wei Zhou,[1] Benxian Peng,[1] Chunqiu Zhang,[1] Xue-Feng Zhu,[2,1,*] Long Meng,[1,3,†] and Hairong Zheng[1,‡]

[1] *Key Laboratory of Biomedical Imaging Science and System, Chinese Academy of Sciences, Shenzhen, Guangdong 518055, China*

[2] *School of Physics and Innovation Institute, Huazhong University of Science and Technology, Wuhan, Hubei 430074, China*

[3] *College of Medicine and Biological Information Engineering, Northeastern University, Shenyang, Liaoning 110016, China*

(Received 12 October 2023; revised 15 November 2023; accepted 16 November 2023; published 1 December 2023)

Noninvasive surface-acoustic-wave (SAW) tweezers provide a powerful tool for on-chip object manipulation. However, the piezoelectric materials for generating SAWs are anisotropic with misaligned directions of wave momenta and energy flow, making the conventional interdigital transducer (IDT) inappropriate for perfect SAW control. Here we propose a holographic IDT for phase-velocity engineering, which improves the focusing quality of SAWs with smaller focal size, larger enhancement of intensity, and precise control of focal position. For the holographic IDT, the focal size is approximately 78.2 μm at 40 MHz, which is 36% smaller than the one produced by a circular IDT. About twofold enhancement of focal intensity and focal length of 10λ are further demonstrated for our design. Nonetheless, we show that the holographic SAW tweezers can implement accurate sorting for solid objects of different sizes as well as large active deformation for liquid droplets even at relatively low input power, which have important biomedical applications.

DOI: 10.1103/PhysRevApplied.20.064003

I. INTRODUCTION

Acoustic tweezers were invented by exchanging acoustic wave momenta with microscopic and/or macroscopic objects to generate a nontrivial force effect that can remotely manipulate solid particles and liquidlike droplets or cells, which showcased important applications in biomedical engineering, material synthesis, and microfluidic chips [1–12]. In general, acoustic tweezers can be realized based on bulk acoustic waves and surface acoustic waves (SAWs), the SAW-based tweezers having attracted intense attention recently for microfluidic applications. Specifically, with the unique features of localized ultrasound fields on the surface and the miniatured device fingerprint, SAW-based acoustic tweezers can be utilized in a wide range of applications such as particle and cell manipulation [13–16], exosome isolation [17–19], and droplet driving, atomization, and jetting [20–23].

As we know, SAWs can be generated by using an interdigital transducer (IDT) on a piezoelectric substrate. By designing different configurations of IDTs, one can realize various SAW fields. For example, a straight IDT can generate plane SAWs [24–26] and a curved IDT can generate focusing SAWs [27,28]. However, a piezoelectric material with a noncentrosymmetric crystal structure is anisotropic, for which the wave vector $\vec{k}$ and energy flow $\vec{v_e}$ of the SAW do not have the same direction [29], making the precise control of SAWs difficult if we do not consider the factor of anisotropy. For example, a circular IDT cannot generate a perfect focus in terms of the anisotropic propagation of SAWs. The deflection of focal position and the augmenting of the focal spot are unavoidable [30,31]. Therefore, there exists an urgent demand for eliminating the deleterious effect of piezomaterial anisotropy, enabling precise SAW field control for functional object manipulation even under a low-input-power condition [32].

In this Paper, we develop a unique type of holographic SAW tweezers, for which the IDTs are modified by considering the anisotropy of SAW propagation in order to generate perfect SAW focusing with a smaller focal spot than previously. We first measured the angular phase-velocity distribution of 128° Y-cut $LiNbO_3$ by using 12 pairs of IDTs oriented in different directions with an interval of 15°. Based on the measurement result, we designed and fabricated the holographic IDT by modifying the electrode configurations to ensure that the direction of

*xfzhu@hust.edu.cn
†long.meng@siat.ac.cn
‡hr.zheng@siat.ac.cn

SAW momentum is consistent with the energy flow. Our approach realized a focusing SAW beam (focal length $\sim 10\lambda$) with the full width at half magnitude (FWHM) being 78.2 μm at 40 MHz, which is 36% smaller than the one generated by a conventional circular IDT. An approximately twofold enhancement of focal intensity was achieved. For the demonstration in potential applications, we used the holographic IDT to implement the precise sorting of microparticles of different sizes under a low input power. Nonetheless, we demonstrate that the focused SAW field generated by the holographic IDT can induce large deformation of microdroplets, which is important for droplet driving, atomization, and jetting.

II. RESULTS AND DISCUSSION

A. Anisotropic properties of $LiNbO_3$

Figure 1(a) illustrates the principle for particle sorting based on the focused SAW from the holographic IDT. To implement the precise sorting of objects with different sizes, high-quality SAW focusing is very important. However, a conventional circular IDT is not the perfect candidate for generating high-quality SAW focusing due to the nontrivial anisotropy of the piezoelectric material. Based on the time-reversal method, we adopt the holographic IDT approach to modify the circular IDT, with the degree of deviation (time delay Δt_n) compensating the phase (or wave vector) offsets in terms of anisotropy. The designed holographic IDT actually follows the slowness curve, which can result in much smaller focusing and a larger energy enhancement in comparison with the circular IDT. Figure 1(b) shows the fabricated SAW device sample for particle sorting, which comprises three channels and two sets of IDTs. The three channels consist of one input channel to inject the particles of different sizes and two output channels to collect the particles of smaller and larger sizes, respectively. The two sets of IDTs are straight IDT for aligning the mixed particles in a straight line and holographic IDT for separating the particles into two groups of different sizes.

In our work, the slowness curve of SAWs was measured in experiments for the next step of holographic IDT design. As shown in Fig. 2(a), we employed 12 pairs of straight IDTs oriented in different directions with an interval of 15°. Here the spacing between adjacent gold electrodes should be equal to $\lambda/4$, where λ is the propagation wavelength of SAWs. To ensure measurement accuracy, we used a laser Doppler vibrometer (LDV, UHF-120) to characterize the operation frequency and the wavelength of SAWs. We then calculated the velocity based on this noncontact measurement technique. For example, from the scanned displacement field along the propagation direction, we can calculate the effective wavelength using $\lambda_{\text{eff}} = S_{\text{eff}}/N$, where N is the number of intersection points between the scanned field and reference plane. Figure 2(b) shows the simulated and measured velocities in different directions, where the maximum velocity is approximately 3973 m/s at angles of 0° and 180°, and the minimum velocity is approximately 3590 m/s at angles of 90° and 270°.

The superposition of SAWs propagating in different directions generates a focusing beam on the surface. In order to perfectly focus the SAW at the target position in the anisotropic piezoelectric material, we adopted the time-reversal approach that was used in acoustic holograms to design the IDT. Let us set a virtual "point source" at the focal position. The shape of holographic IDT should coincide with the wave fronts produced by the point source, where the wave vector $\vec{\boldsymbol{k}}$ and energy flow $\vec{\boldsymbol{v_e}}$ should be consistent. To calculate the geometry of the holographic IDT, we need to obtain the angular deflection between the phase velocity and group velocity [31,33]:

$$\Gamma = \tan^{-1}\left(-\frac{\partial k}{k}\right), \tag{1}$$

where $k = \omega/v(\theta)$ is the wave vector and $v(\theta)$ is the phase velocity along each direction θ. In addition, we define an anisotropy parameter γ, which is the partial differentiation

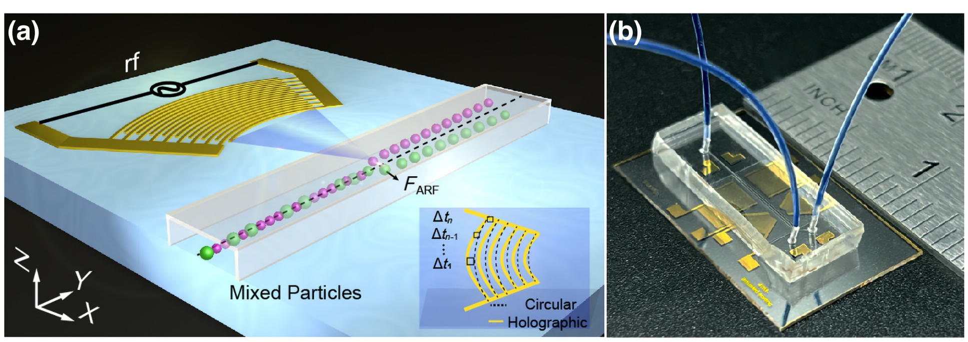

FIG. 1. (a) Precise microparticle separation based on holographic IDT. The inset illustrates the modification (time delay Δt_n) between the circular and holographic IDTs. (b) The SAW-based microfluidic device with holographic IDT.

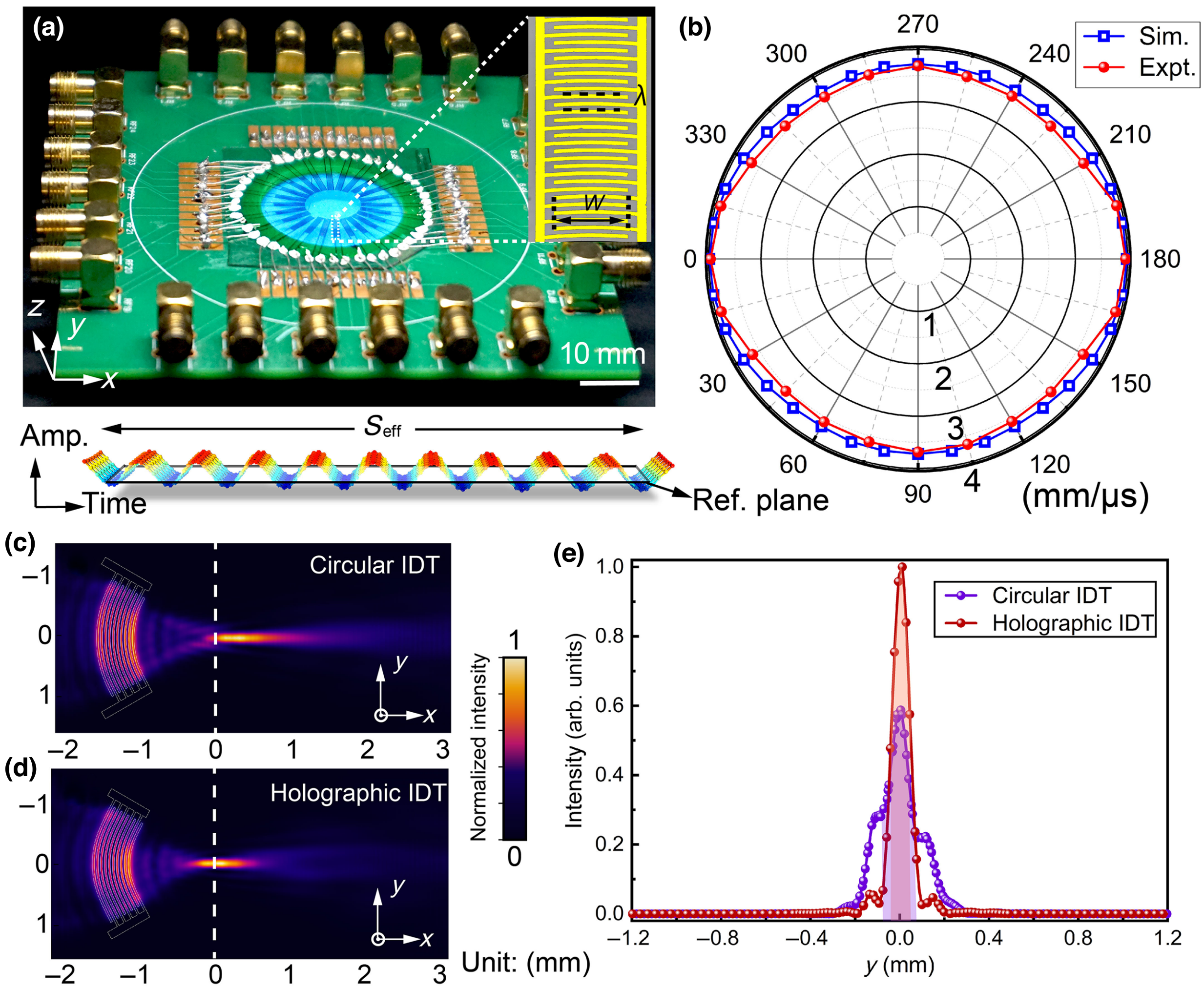

FIG. 2. (a) The fabricated SAW device with 12 pairs of straight IDTs for characterizing the anisotropy of phase velocity. (b) The simulated and measured phase velocities at 40 MHz for SAWs propagating in different directions on the $LiNbO_3$ substrate. Normalized intensity distributions of out-of-plane displacements (z component) for (c) the circular IDT and (d) the designed holographic IDT. (e) Quantitative comparison between the displacement intensity distributions on the dashed lines [at approximately 10λ from the electrodes in (c),(d)], which are generated by the circular and holographic IDTs.

of the deflection angle Γ and the propagation angle θ:

$$\gamma = \frac{\partial \Gamma}{\partial \theta}. \tag{2}$$

For the 128° Y-cut $LiNbO_3$ substrate, the anisotropy parameter in each direction can be calculated from the measured phase velocities in different directions. As shown in Appendix A, the anisotropy parameter suffers from a substantial change in different directions. The geometry of the holographic IDT can thus be calculated from the curvature radius of the metal fingers, which is expressed as

$$R(\theta) = L_m \frac{v(\theta)}{v(\theta = 0)}, \tag{3}$$

where L_m is the focal length for the mth finger and $L_m = L_0 + m\lambda/2$. For the case of $\gamma\theta^2 \leq 1$, the curvature radius $R(\theta)$ can be calculated by

$$R(\theta) = L_m \left(1 + \frac{\gamma}{1+\gamma}\frac{\theta^2}{2}\right). \tag{4}$$

Here, we set L_0 to be the distance from the innermost finger to the predesigned focus and $L_0 = 10\lambda$. λ is the propagation wavelength of SAWs at 40 MHz, which is $\lambda = 100$ μm. The anisotropy parameter γ is determined by the deflection angle and the designed propagation angle in the range of $[0, \pi/6]$. With the information above, the configuration of the holographic IDT can be readily obtained (see Appendix A).

Figure 2(c) shows the normalized intensity distribution of the out-of-plane displacement field (z component) for the circular IDT, with the focus spot at a distance exceeding 10λ. The anisotropy of the $LiNbO_3$ substrate leads to an augmented focal spot. By using the holographic IDT in Fig. 2(d), the SAW focusing is significantly improved with a smaller focal spot and the focal position exactly at 10λ. In Fig. 2(e), we present a quantitative comparison between the focusing performance for circular and holographic IDTs. The transverse intensity fields along the dashed lines in Figs. 2(c) and 2(d) are normalized, where the focal FWHM of the holographic IDT is around 87.7 μm, much smaller than that of the circular IDT (122.77 μm) at the target position (10λ). We further calculate the integral of normalized intensity in the shadowed regions as marked in Fig. 2(e), which are 0.068 and 0.074 for circular and holographic IDTs, respectively, showing an obvious intensity enhancement.

Figure 3(a) illustrates the acoustic setup for measuring the SAW fields via LDV. The out-of-plane displacement of SAWs can be represented by the frequency shift of the reflected laser pulse with respect to the reference light. In the LDV setup, the Nd:YAG laser is focused to a spot size of only 2.5 μm, which determines the resolution of field scanning. Figure 3(b) shows the measured focal spot of SAWs for the circular IDT, for which the maximum position is located in the region around 36λ. Figure 3(c) shows the measured focal spot of SAWs for the holographic IDT, for which the maximum is located at exactly 10λ. In Fig. 3(d), we present a quantitative comparison between the measured FWHMs for the focal spots of circular and holographic cases. Detailed information on the vibration profiles measured by LDV can be found in Video 1. Comparing the transverse intensity field distributions at the maximum positions as marked by the arrows in Figs. 3(b) and 3(c), we find that the measured FWHM for the holographic IDT is 78.2 μm, which is 36.14% smaller than that for the circular IDT (122.45 μm).

B. Microparticle manipulation via holographic SAW tweezers

The holographic IDT is important for SAW-based applications. For example, by bonding a Polydimethylsiloxane (PDMS) layer to the piezosubstrate with the IDT-based alignment and separation modules, we can realize a microfluidic device for particle sorting. In the experiment, an inverted fluorescence microscope (Zeiss Axio Observer 7) was used to analyze the sizes of fluorescent particles. A real-time upright microscope (DM4000B/M, Leica) was

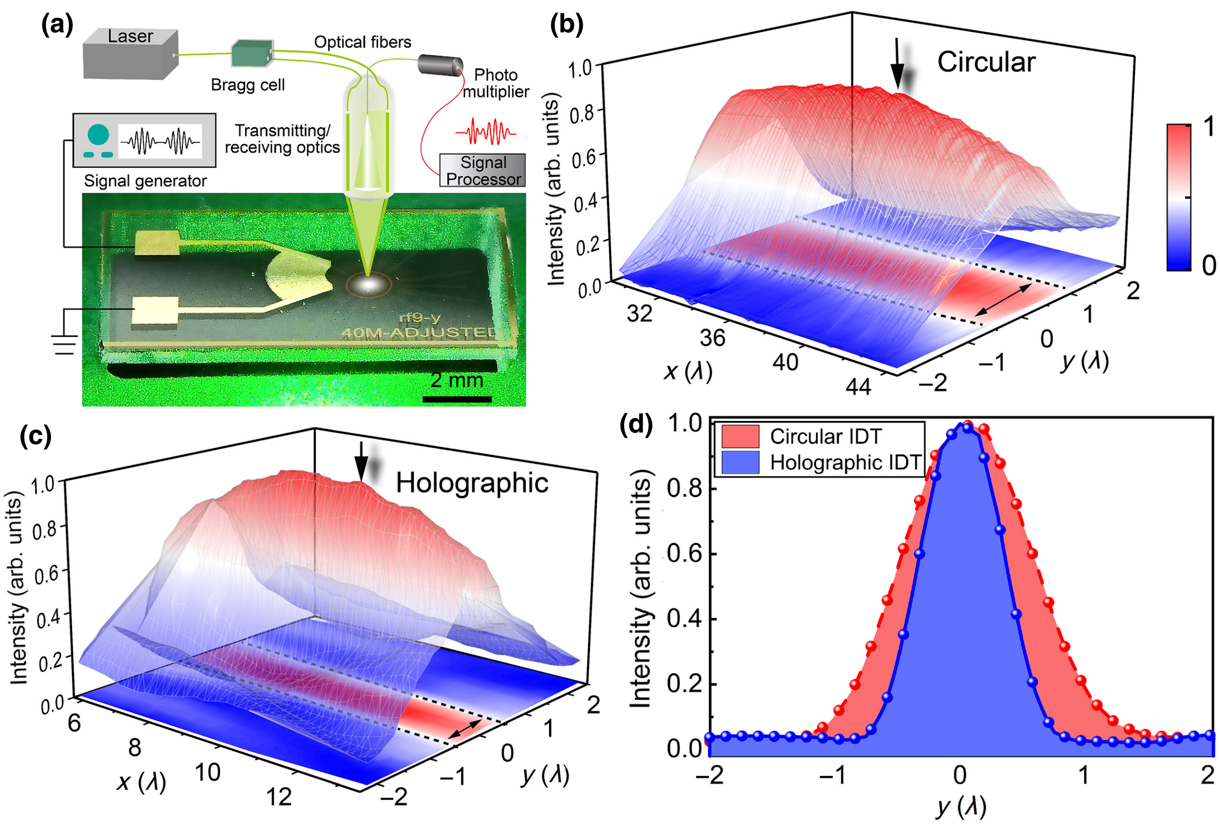

FIG. 3. (a) Schematic of holographic IDT and LDV systems for measuring the SAW fields. The measured out-of-plane vibration intensity distributions for (b) circular and (c) holographic IDTs. The arrows in (b),(c) mark the positions of maximum intensities for the focusing SAW fields created by the circular and holographic IDTs. (d) The measured FWHMs for SAW focusing by circular and holographic IDTs.

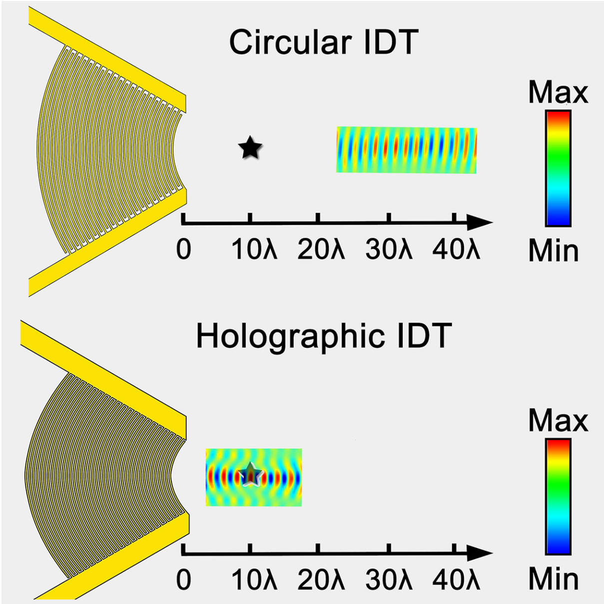

VIDEO 1. Measured out-of-plane vibration field driven by conventional circular IDT and holographic IDT.

used to record the sorting process with a high temporal resolution. A mixture of green (diameter: 5 μm; EGFP) and red (diameter: 2 μm; Rhoda) fluorescent microparticles was used to characterize the sorting performance. The mixed particles diluted in a surface-active agent (F127 solution) with a mixing ratio of 1:2:1 (Rhoda, EGFP, F127) were injected in the channel by a micropump with a flow rate of 10 nl/s. In the acoustic device, the straight IDT in the alignment module (part I) produced a standing wave at 29.88 MHz for aligning the particles via the vibration node into a line, as shown in Fig. 4(a). The aligned particles moved to the separation module by the external flow, where the acoustic radiation force of the holographically focused SAWs acting on the large particles is much larger than that acting on the small particles due to the relation of $F \propto R^6$ [34,35] with R denoting the particle radius. From the relation of $F \propto R^6$, we find that the SAW device has a better performance for the mixed particles with larger size differences. In Fig. 4(b), the fluorescent image clearly shows that the EGFP particles are separated from the Rhoda particles with a separation angle of θ. Figure 4(c) shows the relation between separation angle θ and input powers for the cases of circular and holographic IDTs. The result shows that the holographic IDT outperforms the circular IDT by exerting a much larger acoustic radiation force as the input power is increased. The pronounced separation angle for the holographic IDT is caused by the more localized focal spot and enhancement of SAW energy.

C. Enhanced droplet deformation via holographic tweezers

We show a further application demonstration: liquid object manipulation by the holographic SAW tweezers. In our experiment, a liquid droplet with a volume of 0.2 μl was precisely placed at the focal spot of focusing SAWs. The acoustic setup is presented in Appendix B. The droplet deformation was recorded by a high-speed CCD, where the diameter D and height H of the liquid droplet were utilized to characterize the deformation quantitatively. For the circular IDT in Fig. 5(a), the droplet exhibited an oscillation mode under ultrasound actuation and finally stabilized into a hemiellipsoid one with a small shape change. In Fig. 5(b), the holographic IDT showed a better performance in deforming the liquid object of the same volume into a flattened one with a nontrivial shape change. The sequence animation of droplet deformation with time evolution can be found in Video 2. To quantitatively characterize the droplet shape changes for the two cases, we introduce a scale factor of D/H, which is shown in Fig. 5(c) with its relation to input power and time. We show the variation of D/H in different time frames, which are initial states (power off: 0 mW), actuation states (power on: 250 mW), and final states (power off: 0 mW), which clearly

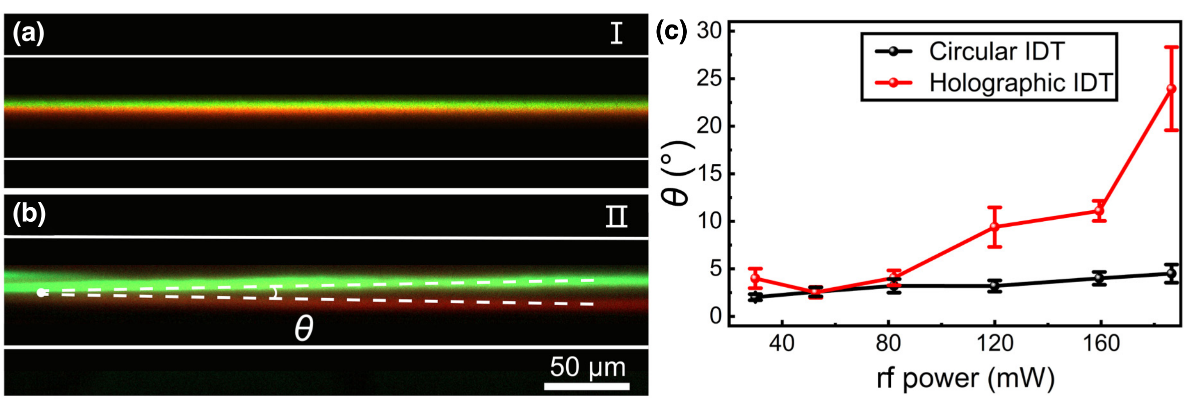

FIG. 4. Snapshots of the bright and fluorescent fields for the (a) aligning module and (b) separating module. (c) The relationship between the separation angle of mixed microparticles and input rf power.

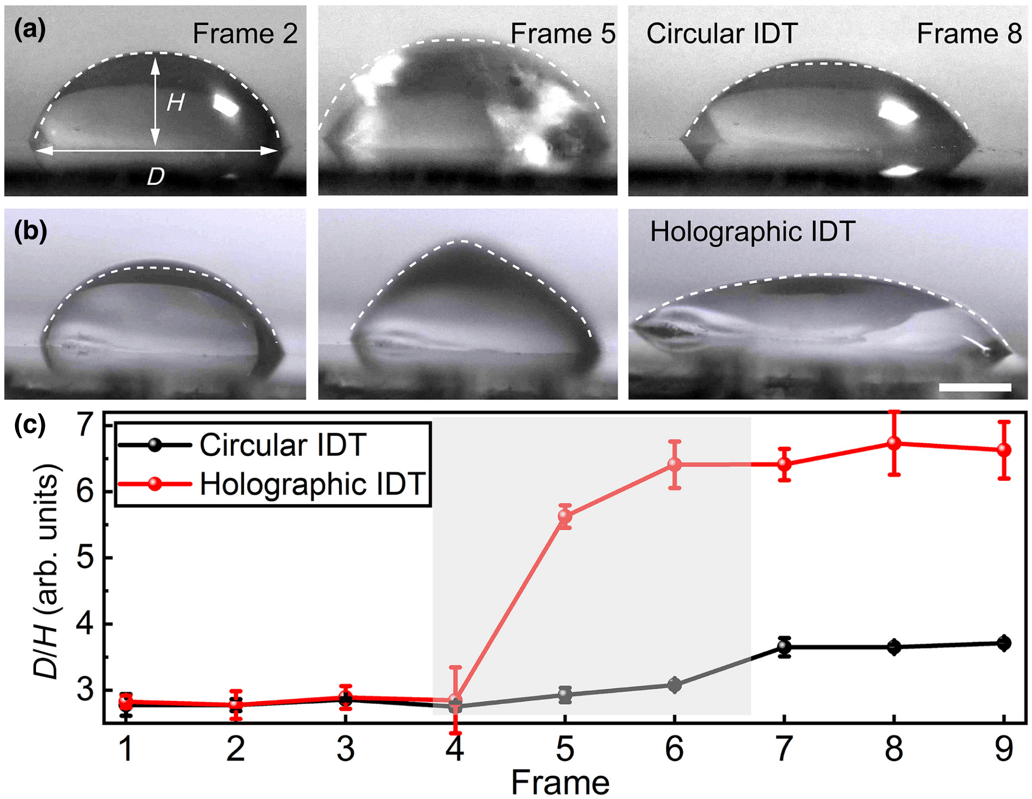

FIG. 5. The real-time deformation of microdroplets (0.2 μl) driven by the (a) circular IDT and (b) holographic IDT. The diameter D and height H of each droplet are marked for characterizing the deformation scale. Scale bar: 1 mm. (c) The measured deformation scale D/H at different time frames, where the gray region indicates the "on" state of power actuation.

demonstrates that the holographic IDT enables a larger deformation of the liquid object than the circular one under the same condition.

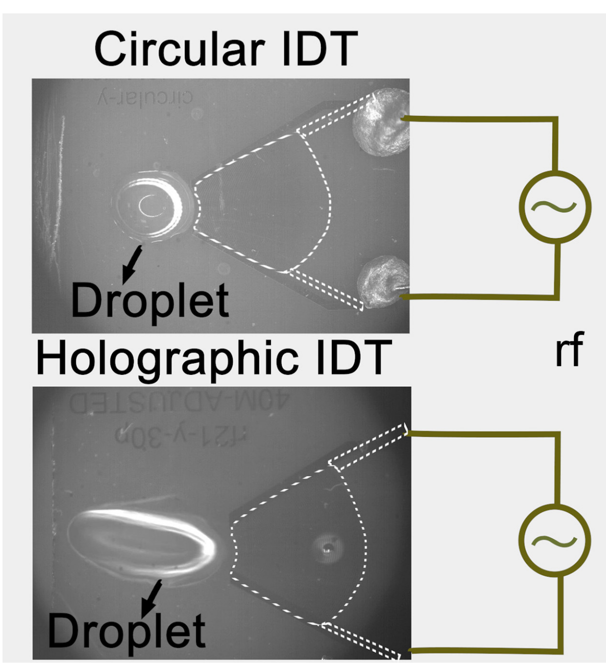

VIDEO 2. Microdroplet deformation process driven by conventional circular IDT and holographic IDT.

III. CONCLUSION

In summary, we have presented a holographic SAW tweezer for functional solid and liquid object manipulation. The principle of the holographic SAW tweezer is based on the time-reversal technique for creating a perfect focal point in anisotropic piezomaterials. With the high-quality localization of SAW energy, the holographic tweezer can achieve precise sorting of solid particles of different sizes as well as large deformation of soft objects even under a low input power. In our experiments, we utilized the holographic IDT to successfully separate 5- and 2-μm particles, for which the particle size plays a key role in the separation process, given the same acoustic properties, such as density and compressibility. By increasing the SAW power above a threshold, the holographic IDT enables a large deformation of droplets, which can transform the mechanical work into heat efficiently and is beneficial for the application of atomization. Our work provides an approach for manipulating SAWs with precise on-chip distribution and large energy density, which is important for microfluidic based applications.

ACKNOWLEDGMENTS

We acknowledge support from the National Key R&D Program of China (Grants No. 2020YFA0211400 and No. 2020YFA0211401), National Natural Science Foundation of China (Grants No. 12022410,

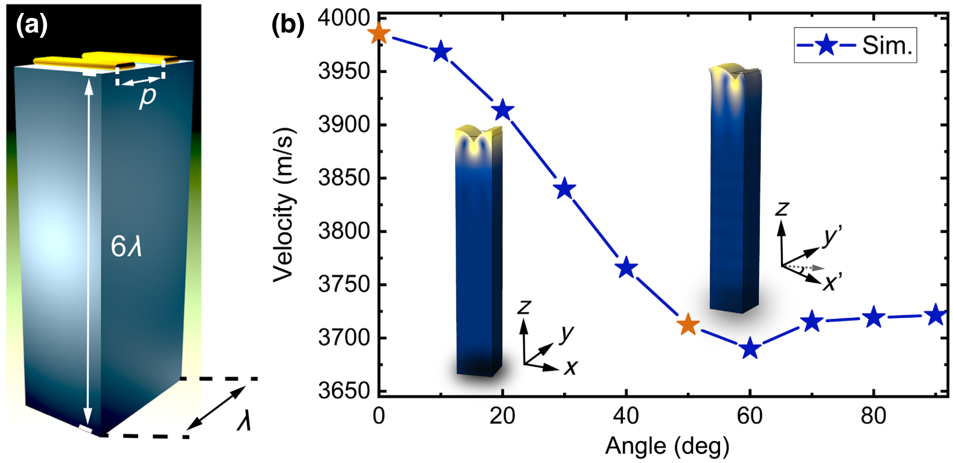

FIG. 6. (a) A schematic of the SAW model used in the finite-element solver to calculate the eigenfrequency, where the thickness of unit cell is 6λ, and the pitch of metal fingers is $p = \lambda/2$. (b) Simulated phase velocities in each direction for the SAW device.

No. 12227809, No. 12104477, and No. T2122023), the Foundation of Chinese Academy of Sciences (YJKYYQ20210019), Natural Science Foundations of Guangdong Province (202381515040008) and Shenzhen Basic Science Research (JCYJ20200109110006136).

APPENDIX A: CHARACTERIZATION OF THE ANISOTROPIC PARAMETERS

Material parameters such as the stiffness tensor, the piezoelectric tensor, and the dielectricity tensor are determined by the cutting of the piezoelectric substrate. Here we choose a 128° Y-cut $LiNbO_3$ substrate and establish the acoustic model in COMSOL Multiphysics 5.5, where the pitch of the IDT is half the wavelength ($p = \lambda/2$). As shown in Fig. 6(a), the substrate thickness is set to be 6λ for preventing reflections from the bottom and the influence of bulk modes. The SAW velocity is calculated by solving the eigenfrequency. Detailed information on 128° Y-cut $LiNbO_3$ used in the simulation can be found in Appendix C. In the simulation, the distribution of phase velocity along each direction can be calculated by sweeping the rotation angle of the unit cell, as shown in Fig. 6(b). The insets present the resonant modes at two different angles of 0° and 50°, for which the eigenfrequencies are 39.86 and 37.12 MHz, respectively, and the phase velocities can be readily obtained since the wavelength is determined.

We can use the measured phase velocities in different directions to calculate the anisotropy parameter γ and the geometric shape of the holographic IDT. In Fig. 7(a), we schematically display the angular deflection between the power flow angle (Γ) and the propagation direction (θ). In Fig. 7(b), we show the angular distributions of the power flow angle (Γ) and the anisotropy parameter γ, which are calculated by Eqs. (1) and (2), respectively. Since in our case the propagation angle of SAWs is set in the range of $[-\pi/6, \pi/6]$, the anisotropy parameter γ is calculated

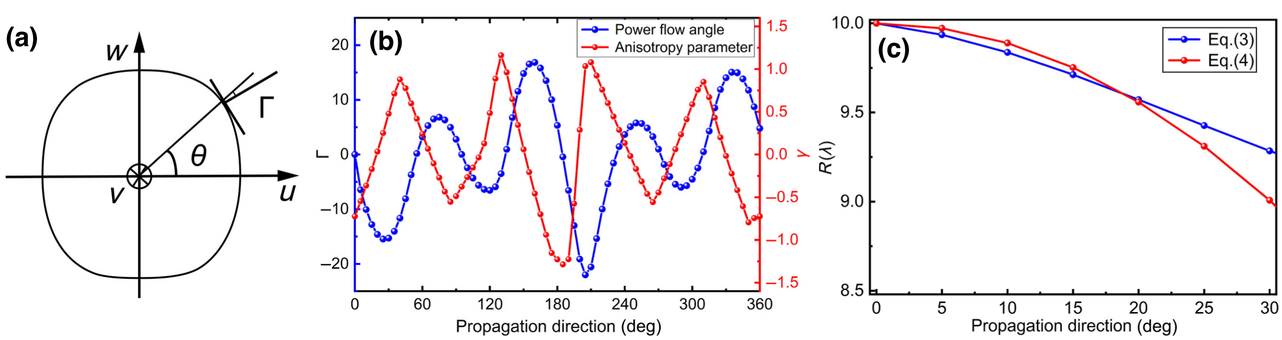

FIG. 7. (a) Schematic for the directions of energy flow and wave momentum for SAWs propagating on the 128° Y-cut $LiNbO_3$ substrate. (b) The power flow angle (Γ) and the anisotropy parameter (γ) in different directions. (c) The curvature radii of IDT fingers versus the propagation angle calculated by Eqs. (3) and (4).

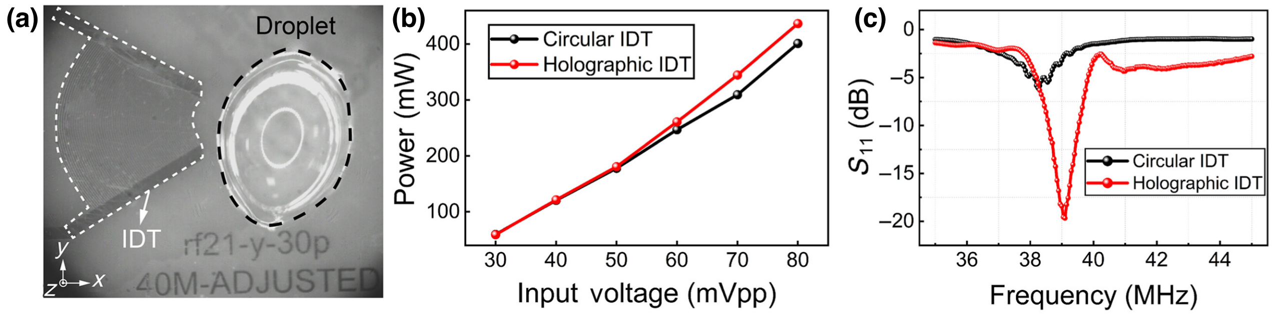

FIG. 8. (a) Top view of the holographic IDT and microdroplet. (b) The measured input power that is applied to the circular and holographic IDTs under different input voltages. (c) The measured $S11$ parameter of the circular and holographic IDTs within the range of 36–44 MHz.

to be within [−1.0, 1.0], as shown in Fig. 7(b), where we find the curvature radius of the IDT calculated by setting $\gamma = -0.41$ in Eq. (4) shows the closest agreement with that calculated by the ideal design rule of Eq. (3), as shown in Fig. 7(c).

APPENDIX B: PERFORMANCE FOR DROPLET MANIPULATION

The droplet-manipulation SAW device is shown in Fig. 8(a). The holographic IDT comprises 30 pairs of metallic electrodes. A high-precision pipette deposits 0.2 μl of degassed water at the focal point precisely. We quantified the power difference between the two methods (circular IDT and holographic IDT). The correlation between the input voltage and input power is shown in Fig. 8(b), which is measured with a power meter. The experiment shows that the proposed holographic IDT provides more efficient energy conversion and has significant acoustically actuated microdroplet deformation in comparison with the circular IDT. Furthermore, we conducted $S11$ measurements for the holographic and circular IDTs at the resonance frequency of around 40 MHz, as shown in Fig. 8(c). The $S11$ values were measured to be −19.564 and −6.094 dB for the holographic and circular IDTs, respectively, which shows enhanced transmission efficiency of the holographic method for the SAW device.

APPENDIX C: PARAMETERS FOR SIMULATION

The crystalline structure of $LiNbO_3$ belongs to the point group of $3m$, which features threefold rotational symmetry about the z axis and the mirror symmetry to the x axis [29]. For $LiNbO_3$ substrates, the stiffness tensor matrix, piezoelectric tensor matrix, and dielectric tensor matrix usually keep in line with the cut of the crystal. We can rotate the crystal axes with Euler angles to align them with Cartesian coordinates in the finite element solver, or just transform the plane matrix through a transformation matrix. In this work, we employ the Bond matrix to perform the transformation for 128° rotated Y-cut $LiNbO_3$. The stress-strain relation is expressed in the stress-charge form by Hooke's law as $\sigma = c_e\varepsilon - e^{\mathrm{T}}E,\ D = e\varepsilon + \varepsilon_0\varepsilon_{rS}E$, where c_e is a 6-by-6 matrix in the Voigt notation. The simplified relation

TABLE I. The parameters used in the numerical simulation.

Elastic stiffness matrix (GPa)					
202.9	70.0	57.8	12.8	0	0
	194.0	90.3	9.0	0	0
		221.2	8.0	0	0
S			75.3	0	0
	Y			56.9	−5.1
		M			77.9

Coupling matrix (C/m^2)						Relative permittivity (1)		
0	0	0	0	0.279	4.472	43.6	0	0
−1.880	4.447	−1.522	0.067	0	0	0	38.126	−7.006
1.715	−2.292	2.314	0.634	0	0	0	−7.006	34.633

can be written as

$$\begin{bmatrix}\sigma_1\\ \sigma_2\\ \sigma_3\\ \sigma_4\\ \sigma_5\\ \sigma_6\end{bmatrix} = \begin{bmatrix} c_{11} & c_{12} & c_{13} & c_{14} & 0 & 0\\ & c_{11} & c_{13} & -c_{14} & 0 & 0\\ & & c_{33} & 0 & 0 & 0\\ S & & & c_{44} & 0 & 0\\ & Y & & & c_{44} & c_{14}\\ & & M & & & (c_{11}-c_{12})/2 \end{bmatrix} \times \begin{bmatrix}\varepsilon_1\\ \varepsilon_2\\ \varepsilon_3\\ \varepsilon_4\\ \varepsilon_5\\ \varepsilon_6\end{bmatrix}, \tag{C1}$$

where c_e are the parameters used in the finite-element solver, $[c_e'] = [M][c_e][N]^{-1}$, M and N being the Bond stress transformation matrix and the strain transformation matrix, respectively. In Table I, we provide the stiffness tensor matrix, piezoelectric tensor matrix, and dielectric tensor matrix used in the finite-element calculation.

[1] Z. Tian, S. Yang, P. H. Huang, Z. Wang, P. Zhang, Y. Gu, H. Bachman, C. Chen, M. Wu, Y. Xie, and T. J. Huang, Wave number-spiral acoustic tweezers for dynamic and reconfigurable manipulation of particles and cells, Sci. Adv. **5**, eaau6062 (2019).

[2] A. Riaud, M. Baudoin, O. Bou Matar, L. Becerra, and J.-L. Thomas, Selective manipulation of microscopic particles with precursor swirling Rayleigh waves, Phys. Rev. Appl. **7**, 024007 (2017).

[3] W. Connacher, N. Zhang, A. Huang, J. Mei, S. Zhang, T. Gopesh, and J. Friend, Micro/nano acoustofluidics: Materials, phenomena, design, devices, and applications, Lab Chip **18**, 1952 (2018).

[4] M. Wu, Y. Ouyang, Z. Wang, R. Zhang, P. H. Huang, C. Chen, H. Li, P. Li, D. Quinn, M. Dao, S. Suresh, Y. Sadovsky, and T. J. Huang, Isolation of exosomes from whole blood by integrating acoustics and microfluidics, Proc. Natl. Acad. Sci. U. S. A. **114**, 10584 (2017).

[5] S. Yang, Z. Tian, Z. Wang, J. Rufo, P. Li, J. Mai, J. Xia, H. Bachman, P. H. Huang, M. Wu, C. Chen, L. P. Lee, and T. J. Huang, Harmonic acoustics for dynamic and selective particle manipulation, Nat. Mater. **21**, 540 (2022).

[6] M. Baudoin, J. C. Gerbedoen, A. Riaud, O. B. Matar, N. Smagin, and J. L. Thomas, Folding a focalized acoustical vortex on a flat holographic transducer: Miniaturized selective acoustical tweezers, Sci. Adv. **5**, eaav1967 (2019).

[7] A. Ozcelik, J. Rufo, F. Guo, Y. Gu, P. Li, J. Lata, and T. J. Huang, Acoustic tweezers for the life sciences, Nat. Methods **15**, 1021 (2018).

[8] L. Meng, F. Cai, F. Li, W. Zhou, L. Niu, and H. Zheng, Acoustic tweezers, J. Phys. D: Appl. Phys. **52**, 273001 (2019).

[9] M. Baudoin, J. L. Thomas, R. A. Sahely, J. C. Gerbedoen, Z. Gong, A. Sivery, O. B. Matar, N. Smagin, P. Favreau, and A. Vlandas, Spatially selective manipulation of cells with single-beam acoustical tweezers, Nat. Commun. **11**, 4244 (2020).

[10] P. Q. Li, Z. L. Li, W. Zhou, S. Wang, L. Meng, Y. G. Peng, Z. Chen, H. Zheng, and X. F. Zhu, Generating multistructured ultrasound via bioinspired metaskin patterning for low-threshold and contactless control of living organisms, Adv. Funct. Mater. **32**, 2203109 (2022).

[11] Z.-L. Li, K. Chen, F. Li, Z.-J. Shi, Q.-L. Sun, P.-Q. Li, Y.-G. Peng, L.-X. Huang, G. Yang, H. Zheng, and X.-F. Zhu, Decorated bacteria-cellulose ultrasonic metasurface, Nat. Commun. **14**, 5319 (2023).

[12] P.-Q. Li, Y.-X. Shen, Z.-G. Geng, P.-C. Cao, Y.-G. Peng, and X.-F. Zhu, Realization of controllable acoustic acceleration beams via flexible active surfaces, J. Phys. D: Appl. Phys. **53**, 155502 (2020).

[13] L. Liu, J. Zhou, K. Tan, H. Zhang, X. Yang, H. Duan, and Y. Fu, A simplified three-dimensional numerical simulation approach for surface acoustic wave tweezers, Ultrasonics **125**, 106797 (2022).

[14] A. Barani, H. Paktinat, M. Janmaleki, A. Mohammadi, P. Mosaddegh, A. Fadaei-Tehrani, and A. Sanati-Nezhad, Microfluidic integrated acoustic waving for manipulation of cells and molecules, Biosens. Bioelectron. **85**, 714 (2016).

[15] N. Korozlu, A. Biçer, D. Sayarcan, O. Adem Kaya, and A. Cicek, Acoustic sorting of airborne particles by a phononic crystal waveguide, Ultrasonics **124**, 106777 (2022).

[16] Q. Liu, Q. Tang, and J. Hu, A new strategy to capture single biological micro particles at the interface between a water film and substrate by ultrasonic tweezers, Ultrasonics **103**, 106067 (2020).

[17] J. Zhang, C. Chen, R. Becker, J. Rufo, S. Yang, J. Mai, P. Zhang, Y. Gu, Z. Wang, Z. Ma, J. Xia, N. Hao, Z. Tian, D. T. W. Wong, Y. Sadovsky, L. P. Lee, and T. J. Huang, A solution to the biophysical fractionation of extracellular vesicles: Acoustic nanoscale separation via wave-pillar excitation resonance (ANSWER), Sci. Adv. **8**, eade0640 (2022).

[18] Y. Yang, L. Zhang, K. Jin, M. H. He, W. Wei, X. J. Chen, Q. R. Yang, Y. Y. Wang, W. Pang, X. B. Ren, and X. X. Duan, Self-adaptive virtual microchannel for continuous enrichment and separation of nanoparticles, Sci. Adv. **8**, eade0640 (2022).

[19] N. Lu, H. M. Tay, C. Petchakup, L. He, L. Gong, K. K. Maw, S. Y. Leong, W. W. Lok, H. B. Ong, R. Guo, K. H. H. Li, and H. W. Hou, Label-free microfluidic cell sorting and detection for rapid blood analysis, Lab Chip **23**, 1226 (2023).

[20] M. H. Biroun, L. Haworth, P. Agrawal, B. Orme, G. McHale, H. Torun, M. Rahmati, and Y. Fu, Surface acoustic waves to control droplet impact onto superhydrophobic and slippery liquid-infused porous surfaces, ACS Appl. Mater. Interfaces **13**, 46076 (2021).

[21] J. Li, M. H. Biroun, R. Tao, Y. Wang, H. Torun, N. Xu, M. Rahmati, Y. Li, D. Gibson, C. Fu, J. Luo, L. Dong, J. Xie, and Y. Fu, Wide range of droplet jetting angles by thin-film based surface acoustic waves, J. Phys. D: Appl. Phys. **53**, 355402 (2020).

[22] S. B. Burnside, K. Pasieczynski, A. Zarareh, M. Mehmood, Y. Q. Fu, and B. Chen, Simulations of surface acoustic

wave interactions on a sessile droplet using a three-dimensional multiphase lattice Boltzmann model, Phys. Rev. E **104**, 045301 (2021).

[23] M. H. Biroun, M. Rahmati, R. Tao, H. Torun, M. Jangi, and Y. Fu, Dynamic behavior of Droplet impact on inclined surfaces with acoustic waves, Langmuir **36**, 10175 (2020).

[24] C. Devendran, D. J. Collins, Y. Ai, and A. Neild, Huygens-Fresnel acoustic interference and the development of robust time-averaged patterns from traveling surface acoustic waves, Phys. Rev. Lett. **118**, 154501 (2017).

[25] L. Meng, X. Y. Cui, C. Y. Dong, X. F. Liu, W. Zhou, W. J. Zhang, X. H. Wang, L. L. Niu, F. Li, F. Y. Cai, J. R. Wu, and H. R. Zheng, Microbubble enhanced acoustic tweezers for size-independent cell sorting, Appl. Phys. Lett. **116**, 073701 (2020).

[26] F. Li, F. Cai, L. Zhang, Z. Liu, F. Li, L. Meng, J. Wu, J. Li, X. Zhang, and H. Zheng, Phononic-crystal-enabled dynamic manipulation of microparticles and cells in an acoustofluidic channel, Phys. Rev. Appl. **13**, 044077 (2020).

[27] K. Wang, W. Zhou, Z. Lin, F. Cai, F. Li, J. Wu, L. Meng, L. Niu, and H. Zheng, Sorting of tumour cells in a microfluidic device by multi-stage surface acoustic waves, Sens. Actuators, B **258**, 1174 (2018).

[28] D. Ahmed, A. Ozcelik, N. Bojanala, N. Nama, A. Upadhyay, Y. Chen, W. Hanna-Rose, and T. J. Huang, Rotational manipulation of single cells and organisms using acoustic waves, Nat. Commun. **7**, 11085 (2016).

[29] B. A. Auld, *Acoustic Fields and Waves in Solids* (Wiley Interscience Pub., New York, 1973), Vol. 1.

[30] J. Rufo, F. Cai, J. Friend, M. Wiklund, and T. J. Huang, Acoustofluidics for biomedical applications, Nat. Rev. Methods Primers **2**, 30 (2022).

[31] R. O'Rorke, A. Winkler, D. Collins, and Y. Ai, Slowness curve surface acoustic wave transducers for optimized acoustic streaming, RSC Adv. **10**, 11582 (2020).

[32] M. B. Schulz, B. J. Matsinger, and M. G. Holland, Temperature dependence of surface acoustic wave velocity on α quartz, J. Appl. Phys. **41**, 2755 (2003).

[33] J. Z. Wilcox and R. E. Brooks, Frequency-dependent beam steering by a focusing array of surface acoustic wave transducers: Experiment, J. Appl. Phys. **58**, 1160 (1985).

[34] A. A. Doinikov, Acoustic radiation forces: Classical theory and recent advances, Recent Res. Dev. Acoust. **1**, 39 (2003).

[35] P. R. Rogers, J. R. Friend, and L. Y. Yeo, Exploitation of surface acoustic waves to drive size-dependent microparticle concentration within a droplet, Lab Chip **10**, 2979 (2010).